Geophysical Research Letters

RESEARCH LETTER
10.1029/2025GL116798

Unraveling the Connection Between Subsurface Stress and Geomorphic Features

B. Kuhasubpasin[1], S. Moon[1], and C. Lithgow-Bertelloni[1]

[1]Department of Earth, Planetary, and Space Sciences, University of California Los Angeles, Los Angeles, CA, USA

Key Points:

- Fault and river flow directions mostly align with Anderson's fault theory predictions based on subsurface stress
- Stresses from lithospheric variations better predict extensional faults, while ones from mantle flow predict compressive faults
- We propose a metric to quantify how mantle flow versus lithospheric heterogeneity shapes surface features, revealing lithospheric strength

Supporting Information:

Supporting Information may be found in the online version of this article.

Correspondence to:

B. Kuhasubpasin,
boontigan@ucla.edu

Citation:

Kuhasubpasin, B., Moon, S., & Lithgow-Bertelloni, C. (2025). Unraveling the connection between subsurface stress and geomorphic features. *Geophysical Research Letters*, *52*, e2025GL116798. https://doi.org/10.1029/2025GL116798

Received 30 APR 2025
Accepted 18 SEP 2025

Author Contributions:

Conceptualization: B. Kuhasubpasin, S. Moon, C. Lithgow-Bertelloni
Formal analysis: B. Kuhasubpasin
Funding acquisition: B. Kuhasubpasin, S. Moon, C. Lithgow-Bertelloni
Investigation: B. Kuhasubpasin, S. Moon, C. Lithgow-Bertelloni
Methodology: B. Kuhasubpasin, C. Lithgow-Bertelloni
Project administration: B. Kuhasubpasin, S. Moon, C. Lithgow-Bertelloni
Resources: C. Lithgow-Bertelloni
Supervision: S. Moon, C. Lithgow-Bertelloni
Validation: S. Moon, C. Lithgow-Bertelloni

Abstract The tectonic stress field induces surface deformation. At long wavelengths, both lithospheric heterogeneity (changes in the thickness and density of crust and lithospheric mantle) and basal tractions from mantle convection contribute to the stress field. Here, we analyze the global alignment of principal horizontal tectonic stresses, fault traces, and river flow directions to infer whether and how deep subsurface stresses control geomorphic features. We find that fault trace orientations are consistent with predictions from Anderson's fault theory. River directions largely align with fault traces and partly with stresses. The degree of alignment depends on fault regime, the source of stress, and river order. Extensional faulting is best predicted by stresses from lithospheric structure variations, while compressive faulting is best predicted by stresses from mantle flow. We propose a metric to quantify the relative influence of mantle flow or lithospheric heterogeneity on surface features, which provides a proxy for lithospheric strength.

Plain Language Summary The state of stress of the lithosphere affects, perhaps even controls, surface deformation. However, how much of the deformation reflects differences in the thickness and density of the crust and lithospheric mantle versus the forces exerted at the base of the lithosphere by the convecting mantle remains a topic of debate and controversy. In this study, we compare the directions of horizontal tectonic stresses, fault lines, and river flow patterns on a global scale to test if and how deep stresses shape these geomorphic features. We separately consider tectonic and topographic controls on river orientation. We found that these three features generally show spatial correspondence: fault traces follow the prediction from Anderson's fault theory, and river directions largely align with fault traces and partly with stresses. However, the degree of correspondence varies based on the fault types, the sources of stress, and the size of the rivers. Extensional faults are mainly influenced by changes in the lithosphere's density and thickness, while compressional faults are more affected by mantle flow. We propose a way to measure the relative impact of mantle flow and lithospheric differences on generating surface features, which may help explain variations in lithospheric strength.

1. Introduction

Earth's surface topography results from the complex interplay between tectonic forces, erosion, and deposition over time (Champagnac et al., 2012; Koons et al., 2012). The subsidence, uplift, and deformation of the lithosphere driven by stresses from Earth's internal dynamics give rise to faults, mountains, seas, and basins (Zoback, 1992; Zoback & Burke, 1993). Erosion driven by gravity, wind, water, and ice reflects environmental conditions such as climate, vegetation, and local lithology (Gilbert, 1880; Hack, 1960). The net outcome of these interactions is the formation of hillslopes, rivers, and valleys (Schumm et al., 2000; Wobus et al., 2006).

That there should be a relationship between faults and stresses is intuitively clear. When stresses exceed the mechanical strength of rocks, they can create large-scale faults and small-scale microcracks and joints (Barton, 1976). The relative magnitudes and orientation of the principal stresses in a given area determine the fault orientation and regime. The traces of normal, strike-slip, and reverse faults are expected to form parallel, acute, and perpendicular to the most compressive horizontal stress orientation, according to Anderson's fault theory (Figure 1) (Anderson, 1905). Fault systems are commonly segmented and propagated, and fractures generated under the same stress field tend to be aligned with each other. Most fractures are created subparallel to major fractures, and fault lines are generally elongated parallel to each other (Nicol et al., 2020).

River flow typically follows surface topography, which reflects the combined influence of surface and subsurface controls, including lithology, climate, tectonics, as well as fluvial network dynamics (Gilbert, 1880; Hack, 1960; Willett et al., 2014; Wobus et al., 2006). Stress-induced surface deformation, including faulting, may influence

Visualization: B. Kuhasubpasin
Writing – original draft: B. Kuhasubpasin
Writing – review & editing: B. Kuhasubpasin, S. Moon, C. Lithgow-Bertelloni

river drainage patterns by shaping topographic relief, providing lateral continuity in accommodation space, or modifying erodibility, to create preferential river paths (Gagliano et al., 2003; Molnar et al., 2007) (Figure 1). Different fault regimes influence river networks in different ways, with strike-slip faults resulting in horizontal offset streams or river captures, and normal and reverse faults influencing the spatial variation of surface uplift, resulting in changes to the river profile and network (Duvall et al., 2020; Lavé & Avouac, 2001; Wobus et al., 2006). Local field studies show that faults and rivers often align (Duvall et al., 2020; Gagliano et al., 2003; Vita-Finzi, 2012). For example, the Mississippi River is bent when crossing the New Madrid fault zone (Gagliano et al., 2003; Vita-Finzi, 2012), and rivers in the Marlborough fault region in New Zealand flow parallel to faults, especially older ones (Duvall et al., 2020).

At length scales beyond the flexural wavelength, the state of stress of the lithosphere is predominantly influenced by variations in its structure - the thickness and density of the crust and lithospheric mantle - and by the net basal tractions resulting from sublithospheric mantle flow (Bird et al., 2008; Lithgow-Bertelloni & Guynn, 2004; Neres et al., 2018; Reiter, 2021; Zoback, 1992) (Figure 1). Deviations from a lithostatic reference state defined by an oceanic column, due to changes in density and thickness of the crust and lithospheric mantle give rise to lateral variations in the gravitational potential energy (GPE). The GPE variations are distributed throughout the lithospheric column, generate outward tractions that act on neighboring columns, and are balanced by gradients in the tectonic stress (Fleitout & Froidevaux, 1983; Ghosh et al., 2008; Lithgow-Bertelloni & Guynn, 2004). At the base of the lithosphere, vertical and horizontal tractions from mantle flow act to either deflect the surface directly, leading to dynamic topography, or drive plate motions (Ghosh et al., 2008; Lithgow-Bertelloni & Guynn, 2004). How these sources of tectonic stress affect the surface deformation will depend on the rheological properties within and below the lithosphere (Lithgow-Bertelloni & Guynn, 2004; Naliboff et al., 2012; Wang et al., 2008).

As the structure of the lithosphere, mantle flow, and rheological properties vary geographically, surface features such as fault traces and river flow directions might reflect those variations, although perhaps not always as expected. For example, given the magnitude of the tectonic stress resulting from mantle flow compared to that from GPE variations, contributions from the former should dominate the field (Ghosh et al., 2008; Ghosh & Holt, 2012; Lithgow-Bertelloni & Guynn, 2004), absent geographical variations in material properties. GPE contributions would only be dominant in orogenic regions or where mantle tractions are small. This is not the case (Kendall & Lithgow-Bertelloni, 2016). The deviations from these expectations cannot be understood in terms of simple tectonic generalizations or variations in asthenospheric viscosity (Naliboff et al., 2009). In other words, active tectonics and high topography regions are not exclusively dominated by contributions from lithospheric heterogeneity. In central and southeast Asia, the contribution from mantle flow is crucial for reproducing the observed overall regional regime pattern and rotation of azimuths of the most compressive principal stress based on the models and seismic observations (Lithgow-Bertelloni & Guynn, 2004; Nábělek et al., 2009). In the East African rift, while GPE contributions provide a better fit to observations of GPS velocities (Stamps et al., 2014), mantle tractions from active upwellings cannot be neglected (Kendall & Lithgow-Bertelloni, 2016). How the relationship between the state of stress, stress sources, and surface features vary locally or globally remains largely unexplored. Filling this gap may provide valuable hints on the spatial variation of tectonic forces and rheological properties of the lithosphere and how those forces manifest themselves at the surface.

In this study, we investigate the connection between present-day subsurface stress and surface geomorphic features, such as fault traces and river flow directions, using observational data and idealized models of present-day tectonic stress. We consider tectonic and topographic contributions to river orientations, while recognizing that other factors (e.g., climate, lithology, and gravity) will influence surface features. While surface features may reflect past stress conditions, we assume that the slow evolution of convective currents in the mantle and the relative stability of lithospheric thickness and composition make it possible to draw meaningful comparisons based on today's lithospheric stress fields. To quantify this connection, we first examine the angles between observed stress directions, fault strikes, and river flow directions, assessing whether they align with Anderson's fault theory. Next, we analyze the relationship between surface features and stresses from different sources, such as mantle flow or lithospheric heterogeneity to assess their relative influence. Lastly, we introduce a metric to quantify the degree of mantle influence on the formation of surface features and discuss its potential to reflect spatial variations in lithospheric strength.

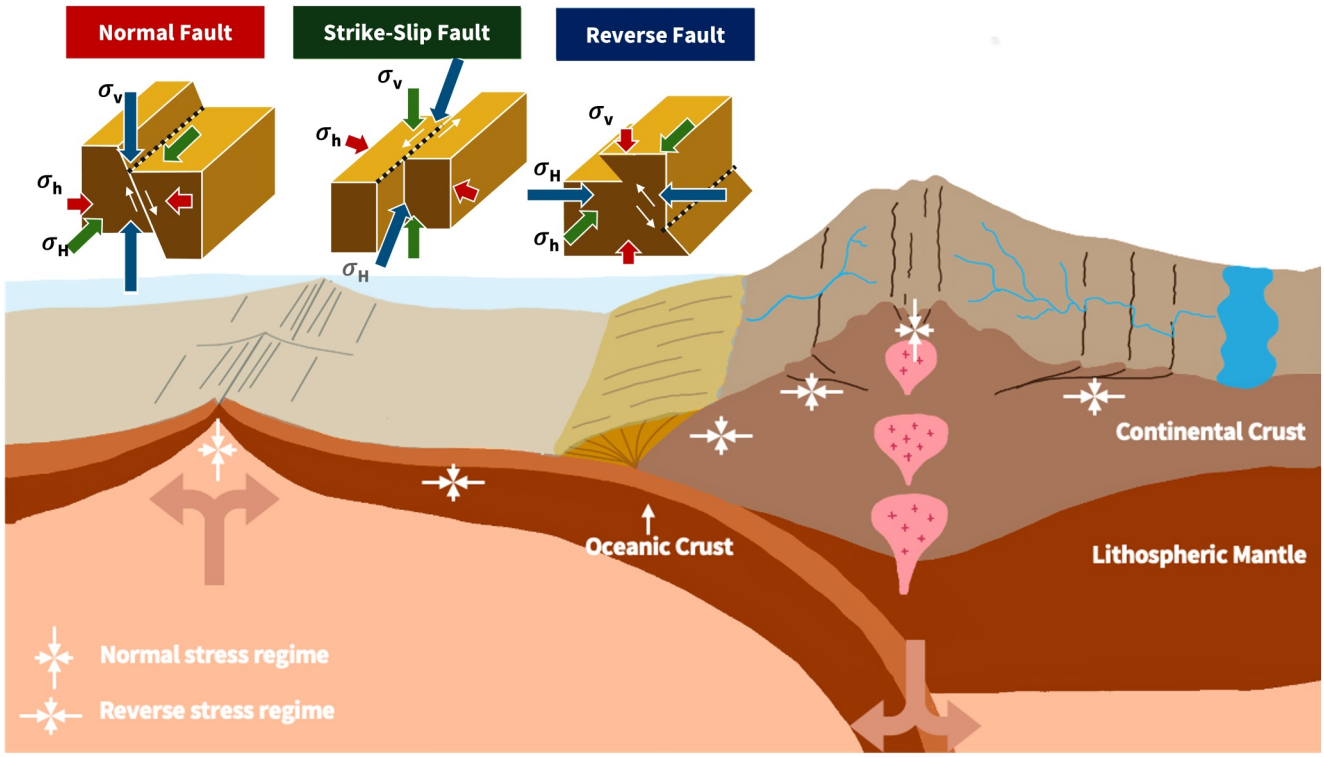

Figure 1. Sources of tectonic stress and their relationship to faults and rivers. The figure shows an idealized cross-section of the lithosphere and convecting mantle across plate margins. Oceanic crust, continental crust, and lithospheric mantle are in light brown, dark beige, and dark brown, respectively. Tractions need not be only parallel or antiparallel to the direction of plate motions (Lithgow-Bertelloni & Guynn, 2004). White arrows indicate the direction and relative magnitude of the most and least compressive stresses expected in each region. Fault traces on continents are shown by thin black lines, river networks by curvy blue lines. The top-left inset illustrates active fault traces for normal, strike-slip, and reverse faults as black dashed lines, together with the corresponding principal stresses (σ_H for the most compressive horizontal stress, σ_h for the least compressive horizontal stress, and σ_V for the vertical stress).

2. Materials and Methods

We obtain the azimuth of the most compressive horizontal stress from observations (σ_{HO}), the fault strike (F), and river flow direction (R) from existing databases. We use (σ_{HO}) from the World Stress Map 2016 (Heidbach et al., 2018), F from mapped fault traces in the Global Active Faults Database (Styron & Pagani, 2020), and R from HydroSHED (Lehner et al., 2008; Wu et al., 2012) (Text S1 in Supporting Information S1). The principal stress azimuths, fault strike directions, and river flow direction are interpolated to the $1° \times 1°$ grid location for the angular difference analysis (Bird & Li, 1996) (Texts S2 and S3 in Supporting Information S1).

To examine the impact of different sources of stress, this study uses magnitudes, azimuths, and regimes of the principal stresses from four models. First, we consider two idealized end-member models of an elastic lithosphere subject to forcings from either lithospheric heterogeneity (σ_{HL}) or mantle flow (σ_{HM}). The first model (σ_{HL}) represents stress caused by variations in GPE, which arise from differences in topography and crustal or lithospheric thickness without any further enforced isostatic adjustment. We use a structure of the lithosphere derived from Crust 1.0 (Laske et al., 2013), combined with a thermodynamically consistent lithospheric mantle structure (Naliboff et al., 2012; Stixrude & Lithgow-Bertelloni, 2005). The lithosphere is treated as compositionally stratified and limited to 100 km thickness for GPE calculations. The second model (σ_{HM}) captures the stresses generated by flow in the mantle beneath the lithosphere. Mantle convection generates shear tractions at the base of the lithosphere, which can be transmitted through the lithosphere to the surface. This model is based on global mantle flow models driven by either global subduction induced density variations or tomography (Lithgow-Bertelloni & Guynn, 2004), incorporates radial viscosity variations in the mantle, has free-slip boundary conditions at the surface, and enforces no net rotation of the lithosphere. Model resolution is approximately 1° at the surface (Text S5 in Supporting Information S1). Later models (Naliboff et al., 2009) found no discernible effects on the lithospheric stress field from lateral variations of viscosity in the mantle.

Second, we consider two models that combine these two sources of stress to assess their combined effect (σ_{HT} and σ_{HB}). The σ_{HT} model, also from Lithgow-Bertelloni and Guynn (2004), linearly combines the resulting tectonic stress in an elastic lithospheric shell from net basal shear tractions and vertical tractions due to mantle flow and those from lithospheric heterogeneity. The σ_{HB} model, from Bird et al. (2008), computes stresses from lithostatic pressure, side strength, and basal strength for a lithosphere with a rheology based on laboratory-derived flow laws appropriate for large geologic strains, using plate velocities as a measure of fit (Text S6 in Supporting Information S1). The details of the models and our rationale for selecting these models instead of more recent mantle flow models are provided in Text S4–S6 in Supporting Information S1.

We calculate the angular difference (Δ) between the azimuth of the most compressive stress azimuth (σ_H), F, and R on a $1° \times 1°$ grid (Text S7 in Supporting Information S1). We examine the abundance distribution of Δ for different fault regimes (i.e., normal, strike-slip, and reverse), stress source types (i.e., observations, lithospheric heterogeneity, and mantle flow), river orders (1st- and >1st-orders; Text S3 in Supporting Information S1), and crustal types. Considering only geographic orientation without directionality, azimuths from all data vary from 0° to 180°. The calculated Δ ranges from 0° (parallel) to 90° (orthogonal). For ease of comparison, we use 30° intervals to group Δ into 3 bins for near-parallel (Δ_{lo}, 0°–30°), oblique (Δ_{mid}, 30°–60°), and near-orthogonal (Δ_{hi}, 60°–90°) angular differences. The choice of bins is consistent with our criteria for regime determination (Text S2 in Supporting Information S1). We use a Monte Carlo simulation to establish the null result (a random distribution of Δ). We define grouped Δ's to have a prominent peak when the value exceeds the sum of the average and one standard deviation (42%), a threshold defined by the percentage data from Table S1 (Text S7) in Supporting Information S1.

3. Results

3.1. Agreement Between Observed Stresses and Surface Features

The spatial distribution and abundance frequency histograms of Δ between σ_{HO} and fault strike direction (hereafter, $\Delta\sigma_{HO} - F$) are shown in Figures 2a and 2b, respectively. Opacity variations represent low to high $\Delta\sigma_{HO} - F$ for normal (red), strike-slip (green), and reverse (blue) fault areas. We expect, from Anderson's fault theory, most values to be Δ_{lo} in normal, Δ_{hi} in reverse, and Δ_{mid} in strike-slip fault regions. The Δ_{lo} are found in normal fault regions, while high Δ_{hi} are predominant in strike-slip and reverse fault areas (Figure 2a and Table S1 in Supporting Information S1). For normal and reverse fault areas, the frequency abundance shows that F tends to be parallel for normal (56% in Δ_{lo}) and perpendicular for reverse (73% in Δ_{hi}) to the σ_{HO}, as expected from Anderson's theory. For strike-slip faults, however, Δ_{hi} (51%) is the most common value rather than the expected Δ_{mid} (32%) (Figure 2b). We find that the observed alignment trends between $\Delta\sigma_{HO} - F$ are generally consistent with Anderson's theory, regardless of depth ranges and measurement techniques used for σ_{HO} (see Figure S1 and Text S1 in Supporting Information S1). One exception is an unclear trend in the normal fault regime at depths greater than 20 km.

The Δ between σ_{HO} and the river flow direction (hereafter, $\Delta\sigma_{HO} - R$) for rivers >1st-order are shown in Figure 2c. For reverse fault areas, the frequency abundance shows that R tends to be perpendicular (41% in Δ_{hi}) to the σ_{HO}. For normal and strike-slip faults, Δ_{mid} (38%) and Δ_{hi} (41%) are the most common values, respectively (Table S1 in Supporting Information S1). We find general agreement between $\Delta\sigma_{HO} - R$ and $\Delta\sigma_{HO} - F$ especially in strike-slip and reverse fault areas, although the prominent peaks in $\Delta\sigma_{HO} - R$ are not as obvious as those in $\Delta\sigma_{HO} - F$.

The abundance frequency histograms of Δ between fault (F) and river (R) azimuths (hereafter, $\Delta F - R$) are shown in Figures S2a and S2c in Supporting Information S1. In normal and strike-slip areas, 43% of the data lie within the lowest angular bin Δ_{lo}, while in reverse areas as much as 47% (Table S1, Figures S2a and S2c in Supporting Information S1). This parallel trend is also visible in Figure 2d, where $\Delta F - R$ and $\Delta\sigma_{HO} - F$ are jointly compared. Higher-density regions (i.e., areas of more opaque color) cluster in the lower part of the plot, corresponding to low $\Delta F - R$ indicative of alignment between faults and rivers in strike-slip and reverse fault regimes; this clustering is not apparent for normal faults. However, if we examine 1st-order rivers, the frequency distributions of $\Delta F - R$ are uniform across all the regimes (Figure S2d in Supporting Information S1).

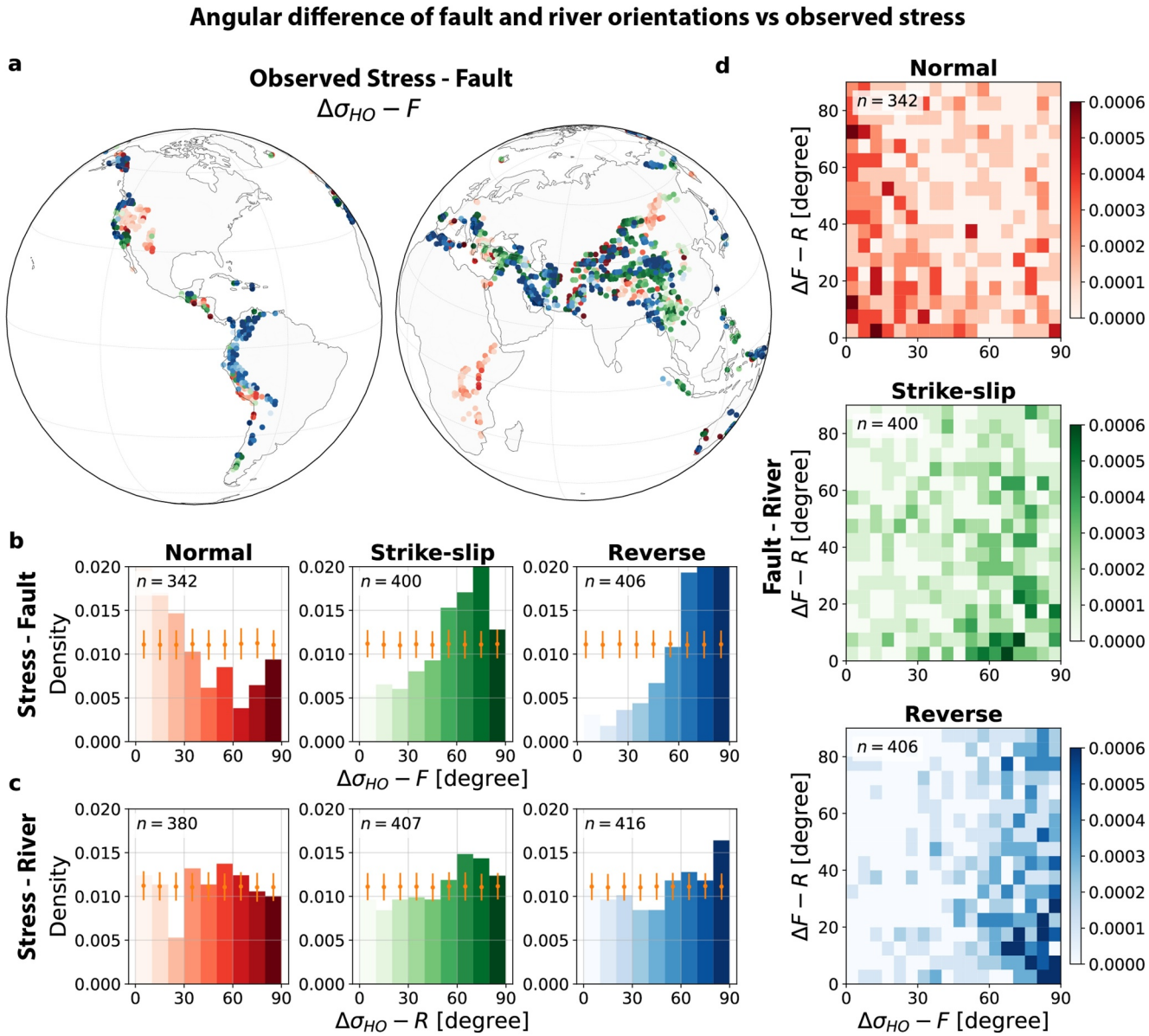

Figure 2. Angular differences (Δ) among observed stress (σ_{HO}), fault strike (F), river flow direction (R). (a) Map of $\Delta\sigma_{HO} - F$ in areas of active faulting. (b) Abundance frequency distribution of $\Delta\sigma_{HO} - F$ with 10° bin intervals. (c) Abundance frequency distribution of $\Delta\sigma_{HO} - R$ with 10° bin intervals. Fault regimes are based on the kinematics of mapped active faults in different colors, normal (red), strike-slip (green), reverse (blue). Color opacity represents low (parallel) to high (perpendicular) Δ. Yellow dots show the range of distribution expected from Monte Carlo simulations. (d) Joint 2D histogram of $\Delta\sigma_{HO} - F$ (x-axis) versus $\Delta F - R$ (y-axis) for >1st-order rivers, showing normalized probabilities. Grid spacing of 5°. Total grid points used in each panel are indicated by n in the top corner.

3.2. Fit and Misfit Between Modeled Stresses and Surface Features

The abundance frequency histograms of Δ between the modeled stresses $(\sigma_{HL}, \sigma_{HM}, \sigma_{HT}, \sigma_{HB})$ and F are shown in Figure 3 and Figure S3 and Table S1 in Supporting Information S1. For lithospheric heterogeneity, the frequency abundances in normal and strike-slip fault areas show that F tends to be parallel (44% in Δ_{lo}) or oblique (39% in Δ_{mid}) to the σ_{HL}, as expected. For reverse faults, however, Δ_{mid} is the most common value rather than the expected Δ_{hi} (Figures 3a and 3e). For mantle flow, the frequency abundance in reverse fault areas shows that F tends to be perpendicular (49% in Δ_{hi}) to the σ_{HM}, again as expected. For normal and strike-slip faults, however, Δ_{mid} and Δ_{hi} are the most common values rather than the expected Δ_{lo} and Δ_{mid} (Figures 3b and 3f). For the modeled stress combining the influence of lithospheric heterogeneity and mantle flow (σ_{HT}, σ_{HB}), both of them show the peak in

10.1029/2025GL116798

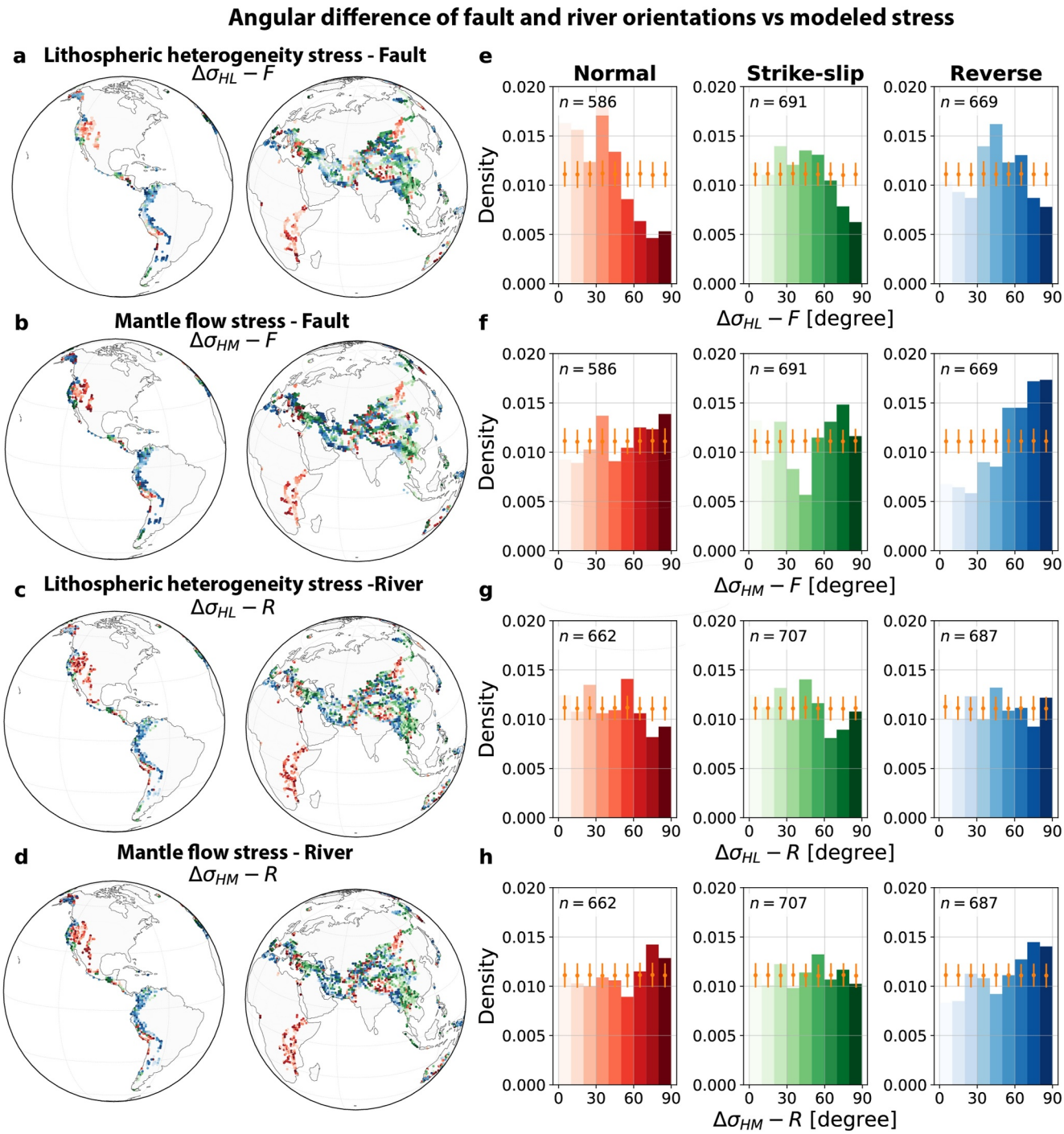

Figure 3. Angular difference of fault and river orientations versus end-member modeled stress (a–d) Maps of Δ for the two end-member models: (a) $\Delta\sigma_{HL} - F$ (lithospheric-heterogeneity stress vs. faults), (b) $\Delta\sigma_{HM} - F$ (mantle-flow stress vs. faults), (c) $\Delta\sigma_{HL} - R$ (lithospheric-heterogeneity stress vs. rivers for >1st-order rivers), and (d) $\Delta\sigma_{HM} - R$ (mantle-flow stress vs. rivers for >1st-order rivers) (e–h) Corresponding abundance frequency distributions (10° bins) for panels (a–d), respectively. Fault regimes based on the kinematics of mapped active faults in different colors, normal (red), strike-slip (green), reverse (blue). Color opacity represents low (parallel) to high (perpendicular) Δ. The total number of grid points used in each panel is indicated by n in the top corner. Yellow dots show the range of distributions expected from Monte Carlo simulations ($n = 1000$) assuming a uniform distribution.

Δ_{lo} for normal faults and the peak in Δ_{hi} for reverse faults (Figures S3a, S3b, S3e and S3f) in Supporting Information S1.

The abundance frequency distributions of Δ between the modeled stress and river flow direction (R) (hereafter, $\Delta\sigma_H - R$) for rivers of higher than >1st-order are relatively uniform (Figures S3 in Supporting Information S1). Most distributions lack prominent peaks. An exception is Δ_{hi} from $\Delta\sigma_{HM} - R$ in reverse faults (43%; see Figure 3h and Table S1 in Supporting Information S1).

In regions without faults, we examine $\Delta\sigma_H - R$ using crustal types from Earth Crustal Model 1 (ECM1) (Text S1 in Supporting Information S1). Although most of the data do not show consistent patterns, $\Delta\sigma_H - R$ from observed and modeled stresses that include lithospheric heterogeneity tend to show the peak in Δ_{lo} in the extended crust region, indicating being parallel (Figure S4 and Table S2 in Supporting Information S1).

4. Discussion

4.1. Spatially Varying Subsurface Stress-Fault Connections Driven by Stress Sources

We find that Anderson's fault theory (Anderson, 1905) is a good predictor of the orientation of fault strikes (Figures 2a and 2b) when comparing to the observed stress σ_{HO}. In regions of normal faulting, σ_{HO} is parallel to the fault strike direction. For reverse regime areas, σ_{HO} is largely perpendicular. Strike-slip faults deviate from the expectations from Anderson's fault theory. These findings validate our null hypothesis that fault orientations are good indicators of the present-day stress field, not only locally, but on a global scale.

To better understand the differences in orientations across fault regimes, we look further into the relationship between fault strike and σ_H using end-member models for each stress contribution. Lithospheric heterogeneity (σ_{HL}) and mantle flow (σ_{HM}) are treated as separate, simplified forcings, while we also use models that combine them. We find that the contributions from lithospheric heterogeneity agree better with Anderson's theory in areas of normal faulting than models from other sources of stress. In regions where reverse faulting is dominant, we see better agreement between fault strike and tectonic stress that result from basal shear traction associated with mantle flow. Both σ_{HT} and σ_{HB} showed some agreement with the prediction in both normal and reverse regimes, similar to the observational stress σ_{HO}. However, the predictions are better when considering the model that treats these two sources of stress separately (i.e., higher percentages in Table S1 in Supporting Information S1).

We can explain this observation in terms of the stress magnitudes to some degree. As the magnitude of tectonic stress induced by mantle tractions is generally much larger than that from lithospheric heterogeneity (Lithgow-Bertelloni & Guynn, 2004) (Figure S5 in Supporting Information S1), this result could just reflect variations in the magnitude of mantle tractions. For example, the excellent agreement in western North America for $\Delta_{HL} - F$ is likely due to small contributions from mantle flow (Lithgow-Bertelloni & Guynn, 2004; Naliboff et al., 2009). As rocks break more easily under tension than under compression, lithospheric-heterogeneity-induced tectonic stress should be more than sufficient to cause normal faulting, even in the absence of large mantle tractions. On the other hand, in areas dominated by reverse faulting, stresses resulting from mantle flow would be essential to overcome the compressive strength of rocks (Griggs, 1936). While stress magnitudes can account for alignment patterns in some regions, this explanation is insufficient because σ_{HT} does not consistently reproduce the observed alignments across all regimes.

4.2. Lithospheric Strength Variations Inferred From Subsurface-Surface Connections

Another plausible explanation is the influence of the geographical variations in lithospheric strength. Variability in lithospheric strength affects how stress manifests at the surface, potentially altering its alignment with surface features. Consequently, the different degrees of alignment between the stress directions of various models and the observed surface features may provide insight into the variations in lithospheric strength.

To quantify how well tectonic stress from mantle flow provides an explanation for generating faults on the surface, we define a metric *MI*, for "mantle influence." Our *MI* metric is based on the misfit of the regime prediction from mantle flow (Reg_M) and lithospheric heterogeneity (Reg_L) compared with the observed fault regime (Reg_F)

$$MI = |Reg_F - Reg_L| - |Reg_F - Reg_M| \quad (1)$$

Reg_L and Reg_M are calculated from the relative magnitude of the principal stresses (Simpson, 1997) and range from 0 (normal) to 1 (reverse). Reg_F is converted from the qualitative data of the fault observations to the same range as a quantitative scale (Text S2 and Figure S6 in Supporting Information S1). The metric ranges from −1 (weak) to 1 (strong), where −1 represents the least match between the regime predicted by mantle flow induced stresses and the regime assigned from fault observations, and 1 represents the greatest match. When two models produce indistinguishable predictions, whether accurate or inaccurate, the *MI* metric will be zero.

Our metric *MI* shows large spatial variation of the relative importance of stress sources and highlights areas where the influence from mantle flow is strong or weak (Figure 4 and Figure S6 in Supporting Information S1). Areas with a strong mantle influence (blue) are found in regions dominated by active reverse faulting, for example, central Europe, western South America, Zagros, and parts of central Asia (Box 1–2 in Figure 4), where stress magnitudes related to mantle flow induced by past and long-lived subduction are large enough to exceed the compressive strength of rocks. Generally, we find weak mantle contributions (red) in regions dominated by active normal faulting, for example, western North America, Mongolia (Box 3 in Figure 4), as expected, given the magnitude of the mantle contributions and the strength of the lithosphere (Clark et al., 2005) (Figure S5 in Supporting Information S1).

There are exceptions to the general agreement between *MI* and tectonic regimes, which support our *MI* metric as an indicator of variations in lithospheric strength (boxes 4–7 in Figure 4). For example, we observe a weak mantle influence in certain areas, for example, central and southeast Asia (Box 4–5 in Figure 4), where based on the magnitude of negative dynamic topography and mantle stresses, we expected strong *MI* (Lithgow-Bertelloni & Guynn, 2004). In eastern Tibet regions, it has been suggested that the lower crust is sufficiently weak to flow (Clark et al., 2005; Yuan et al., 2013). In addition, regions of active reverse faulting, for example, western Europe (Box 6 in Figure 4), that exhibit weak *MI* tend to have a low effective elastic thickness (Audet & Bürgmann, 2011), indicating low strength. Conversely, we observe strong *MI* in a region dominated by extensional tectonics, for example, eastern Africa (Box 7 in Figure 4). This anomaly is likely due to active mantle upwellings and positive dynamic topography, which contribute significantly to present-day rifting (Kendall & Lithgow-Bertelloni, 2016).

To assess the efficacy of our *MI* metric for lithospheric strength, we compare our *MI* metric with effective elastic thickness T_e (Audet & Bürgmann, 2011) on a global scale (Text S1 in Supporting Information S1, Figures 4b and 4c). T_e is estimated from the spectral coherence between topography and Bouguer gravity anomalies and is used as a proxy for the long-term strength of the lithosphere in previous studies (Audet & Bürgmann, 2011). In regions of normal faulting, we observe a positive trend between *MI* and T_e, where higher *MI* values tend to occur in areas with thicker elastic lithosphere (Figure S7 in Supporting Information S1). This suggests that mantle-driven stresses may play an important role where the lithosphere is more resistant to deformation (Figure S7 in Supporting Information S1). While no strong correlation is observed in reverse faulting regions, *MI* values are generally higher in these areas than in extensional regions. This may indicate that a high degree of mantle influence may be required to initiate compressional deformation, potentially because greater lithospheric strength thresholds must be overcome in such a tectonic setting. These findings support the potential utility of our *MI* metric as an indicator of lithospheric strength, which is often hard to measure.

4.3. Limitations and Future Directions

Our findings do not fully explain all observed fault strikes and river flow directions in terms of subsurface stress contributions. Fault strikes generally align with stress predictions, but river flow directions show only partial correspondence, for example, being perpendicular to mantle-driven stress in thrust regimes (Figure 2) and parallel to observed stress in extended crust in inactive areas (Figure S4 in Supporting Information S1).

We acknowledge that river flow is influenced by surface topography, which reflects tectonic, climatic, erodibility, and substrate factors (Gilbert, 1880; Hack, 1960; Schumm et al., 2000; Willett et al., 2014; Wobus et al., 2006). Given our focus on large spatial scales (∼100 km), perfect alignment between stress and river flows was not expected. These scales exceed typical variations in topographic relief, lithology, and fault-related damage.

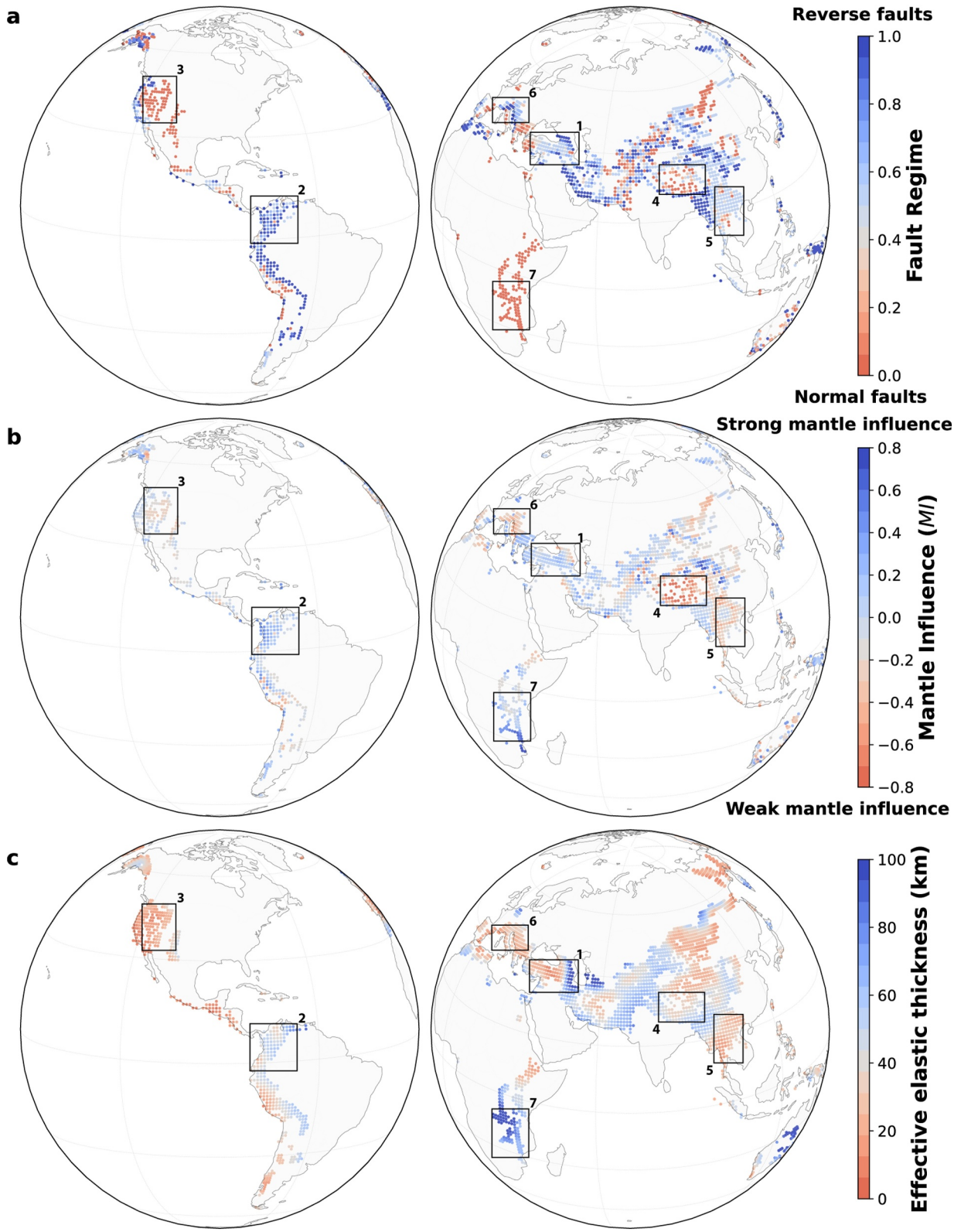

Figure 4.

Supplementary Figure S4 in Supporting Information S1 highlights this complexity, especially in non-active regions where stress–river alignment weakens.

Interestingly, we find stronger alignment between fault strikes and river flow directions in higher-order rivers, regardless of fault regime (Figure S2 in Supporting Information S1), suggesting a global influence of faults on river network development. We acknowledge that we cannot completely isolate tectonics from topographic controls because topography develops across the fault. Indeed, we find that topographic aspect, or the steepest downward slope direction, tends to be perpendicular to fault strike (Supplementary Figures S8a and S8d in Supporting Information S1). Lower-order rivers align with topographic aspect, whereas higher-order rivers align with fault strike (Supplementary Figures S2, S8b, S8c, S8e, and S8f in Supporting Information S1).

We propose that subsurface stress drives surface deformation and subsequently creates preferential flow directions for higher-order rivers through (a) large-scale topographic development, and (b) enhanced erodibility due to fault zone damage or tectonically-induced rock weakening (e.g., earthquake shaking). We see strong evidence for our proposed mechanisms in reverse and strike-slip settings, where topography develops perpendicular to the fault strike (Figure S8 in Supporting Information S1). Instead, for normal faults, the weaker agreement may reflect the more complex ways in which rivers interact with faults under extension. For example, in the Basin and Range, some rivers exploit fault-related weak zones and run parallel to faults, while others are strongly guided by the local topography generated by normal faulting, which tends to be perpendicular to fault traces. This dual control can reduce the overall statistical correspondence compared to strike-slip or reverse settings (Figure 2 and Figure S8 in Supporting Information S1).

In addition, strike-slip faults do not always follow our expectations. However, few strike-slip faults are pure strike-slip (Sylvester, 1988). Many strike-slip faults are either transtensional or transpressional. Subdividing strike-slip faults, we find that transtensional fault histograms resemble normal faults while transpressional histograms resemble reverse ones for the modeled stresses (Figure S9 in Supporting Information S1). This suggests that the additional extensional or compressional components in these mixed regimes potentially reflect the influence of the fault–stress connection. There are other geologic complexities that we did not consider, such as the presence of low effective friction in strike-slip faults, potentially resulting from dynamic lubrication by heated and pressurized pore fluids (Lachenbruch, 1980; Wibberley & Shimamoto, 2005). In the Himalayas, discrepancies between observed and predicted fault directions from Anderson's theory of faulting are likely due to Riedel shearing (Yin & Taylor, 2011).

Future improvements to our methodology will be multi-fold. Incorporating additional geomorphic features, such as fractures, dikes, or joint sets that are controlled by the prevalent state of stress, could provide a better understanding of tectonic stress effects in certain regions. We can also improve the stress models. By moving beyond the GPE approximation, we can explore the full effects of variation in lithology and thickness in the continental lithosphere. Mantle flow models could be improved by incorporating lateral variations in viscosity and rheological laws influenced by damage and grain size, especially at plate boundaries (Bercovici & Ricard, 2012; Foley & Bercovici, 2014; Zhong et al., 2000). Predicted tectonic stresses for both mantle tractions and lithospheric heterogeneity are based on the present-day. Present-day faulting and geomorphic features may in part reflect the imprint of long-lived lithospheric structures and the cumulative effects of mantle flow processes. Their long-term influence provides important context for understanding modern surface deformation, while fully integrating their evolution remains a longer-term goal for future models. Despite its limitations, our spatial analysis provides a novel way to understand how subsurface sources of tectonic stress manifest at the surface and provide an indication of geographical variations in the strength of the lithosphere.

Figure 4. (a) Global map of fault regimes, adapted from the Global Active Faults Database (Styron & Pagani, 2020). Values range from 0 (red) for normal faults, to 0.5 (gray) for strike-slip faults, to 1 (blue) for reverse faults. Details on how these numerical values were assigned from the descriptions in the database are provided in Text S2 in Supporting Information S1.(b) Global map of the degree of influence of mantle flow on surface features, *MI*. The colors represent the strength of influence, ranging from strong (blue) to uncertain (gray) to weak (red). The observed values for this metric vary from −0.8 to 0.8. (c) Global map of effective elastic thickness (T_e) from Audet and Bürgmann (2011), representing lithospheric strength. T_e map displays only the areas where *MI* is defined. Boxes show areas discussed in the main text.

Conflict of Interest

The authors declare no conflicts of interest relevant to this study.

Data Availability Statement

All observational data are available online, including: observed stresses from the World Stress Map 2016 (https://www.world-stress-map.org: Heidbach et al. (2018)), GEM global active faults (https://www.globalquakemodel.org/product/active-faults-database: Styron and Pagani (2020)), HydroSHEDs river flow direction (https://www.hydrosheds.org/products/hydrosheds: Lehner et al. (2008)), Global crustal model (https://igppweb.ucsd.edu/~gabi/crust1.html: Laske et al. (2013) and https://www.earthcrustmodel1.com: Mooney et al. (2023)).

The interpolated data for faults, river networks, and stresses used in this study are available through Kuhasubpasin et al. (2025). Codes used in this work to generate individual results are publicly available and open source through Kuhasubpasin et al. (2025). For further requests, please contact the authors.

Acknowledgments
We thank P. Bird for sharing and discussing the total lithospheric stress modeling and for providing valuable feedback on this manuscript. We also thank J. Naliboff for providing the MATLAB codes to generate the stress fields from lithospheric heterogeneity and G.E.Hilley for discussion. We also acknowledge two reviewers and the editor for constructive feedback, which helped improve the manuscript. This study is supported by the National Science Foundation under Grant EAR-1900633 to C.L-B. and National Science Foundation Grant EAR-1945431, EAR-2012073, and the Alfred P. Sloan Foundation to S.M. C.L-B. was also supported by the Louis B. and Martha B. Slichter Endowed Chair in Geosciences. B.K. is supported by the Anandamahidol Foundation fellowship.

References

Anderson, E. M. (1905). The dynamics of faulting. *Transactions of the Edinburgh Geological Society*, *8*(3), 387–402. https://doi.org/10.1144/transed.8.3.387

Audet, P., & Bürgmann, R. (2011). Dominant role of tectonic inheritance in supercontinent cycles. *Nature Geoscience*, *4*(3), 184–187. https://doi.org/10.1038/ngeo1080

Barton, N. (1976). The shear strength of rock and rock joints. *International Journal of Rock Mechanics and Mining Sciences & Geomechanics Abstracts*, *13*(9), 255–279. https://doi.org/10.1016/0148-9062(76)90003-6

Bercovici, D., & Ricard, Y. (2012). Mechanisms for the generation of plate tectonics by two-phase grain-damage and pinning. *Physics of the Earth and Planetary Interiors*, *202*, 27–55. https://doi.org/10.1016/j.pepi.2012.05.003

Bird, P., & Li, Y. (1996). Interpolation of principal stress directions by nonparametric statistics: Global maps with confidence limits. *Journal of Geophysical Research*, *101*(B3), 5435–5443. https://doi.org/10.1029/95jb03731

Bird, P., Liu, Z., & Rucker, W. K. (2008). Stresses that drive the plates from below: Definitions, computational path, model optimization, and error analysis. *Journal of Geophysical Research*, *113*(B11). https://doi.org/10.1029/2007jb005460

Champagnac, J.-D., Molnar, P., Sue, C., & Herman, F. (2012). Tectonics, climate, and mountain topography. *Journal of Geophysical Research*, *117*(B2), B02403. https://doi.org/10.1029/2011jb008348

Clark, M. K., Bush, J. W. M., & Royden, L. H. (2005). Dynamic topography produced by lower crustal flow against rheological strength heterogeneities bordering the Tibetan Plateau. *Geophysical Journal International*, *162*(2), 575–590. https://doi.org/10.1111/j.1365-246x.2005.02580.x

Duvall, A. R., Harbert, S. A., Upton, P., Tucker, G. E., Flowers, R. M., & Collett, C. (2020). River patterns reveal two stages of landscape evolution at an oblique convergent margin, Marlborough Fault System, New Zealand. *Earth Surface Dynamics*, *8*(1), 177–194. https://doi.org/10.5194/esurf-8-177-2020

Fleitout, L., & Froidevaux, C. (1983). Tectonic stresses in the lithosphere. *Tectonics*, *2*(3), 315–324. https://doi.org/10.1029/tc002i003p00315

Foley, B. J., & Bercovici, D. (2014). Scaling laws for convection with temperature-dependent viscosity and grain-damage. *Geophysical Journal International*, *199*(1), 580–603. https://doi.org/10.1093/gji/ggu275

Gagliano, S. M., Kemp Iii, E. B., Wicker, K., & Wiltenmuth, K. (2003). *Active geological faults and land change in southeastern Louisiana* (Vol. 204). Study for US Army Corps of Engineers.

Ghosh, A., & Holt, W. E. (2012). Plate motions and stresses from global dynamic models. *Science*, *335*(6070), 838–843. https://doi.org/10.1126/science.1214209

Ghosh, A., Holt, W. E., Wen, L., Haines, A. J., & Flesch, L. M. (2008). Joint modeling of lithosphere and mantle dynamics elucidating lithosphere-mantle coupling. *Geophysical Research Letters*, *35*(16), L16309. https://doi.org/10.1029/2008gl034365

Gilbert, G. K. (1880). *Report on the geology of the Henry Mountains* (Vol. 4). US Government Printing Office.

Griggs, D. T. (1936). Deformation of rocks under high confining pressures: I. Experiments at room temperature. *The Journal of Geology*, *44*(5), 541–577. https://doi.org/10.1086/624455

Hack, J. T. (1960). Interpretation of erosional topography in humid temperate regions (Vol. *293*).

Heidbach, O., Rajabi, M., Cui, X., Fuchs, K., Müller, B., Reinecker, J., et al. (2018). The world stress map database release 2016: Crustal stress pattern across scales. *Tectonophysics*, *744*, 484–498. https://doi.org/10.1016/j.tecto.2018.07.007

Kendall, J. M., & Lithgow-Bertelloni, C. (2016). Why is Africa rifting? *Geological Society*, *420*(1), 11–30. https://doi.org/10.1144/sp420.17

Koons, P. O., Upton, P., & Barker, A. D. (2012). The influence of mechanical properties on the link between tectonic and topographic evolution. *Geomorphology*, *137*(1), 168–180. https://doi.org/10.1016/j.geomorph.2010.11.012

Kuhasubpasin, B., Moon, S., & Lithgow-Bertelloni, C. (2025). Unraveling the connection between subsurface stress and geomorphic features Dataset [Collection]. *Zenodo*. https://doi.org/10.5281/zenodo.12620524

Lachenbruch, A. H. (1980). Frictional heating, fluid pressure, and the resistance to fault motion. *Journal of Geophysical Research*, *85*(B11), 6097–6112. https://doi.org/10.1029/jb085ib11p06097

Laske, G., Masters, G., Ma, Z., & Pasyanos, M. (2013). *Update on crust 1.0 – a 1-degree global model of Earth's crust [Conference Proceedings]*. In (Vol. 15, p. 2658). EGU General.

Lavé, J., & Avouac, J. P. (2001). Fluvial incision and tectonic uplift across the Himalayas of central Nepal. *Journal of Geophysical Research*, *106*(B11), 26561–26591. https://doi.org/10.1029/2001JB000359

Lehner, B., Verdin, K., & Jarvis, A. (2008). New global hydrography derived from spaceborne elevation data. *Eos, Transactions American Geophysical Union*, *89*(10), 93–94. https://doi.org/10.1029/2008eo100001

Lithgow-Bertelloni, C., & Guynn, J. H. (2004). Origin of the lithospheric stress field. *Journal of Geophysical Research*, *109*(B1), B01408. https://doi.org/10.1029/2003jb002467

Molnar, P., Anderson, R. S., & Anderson, S. P. (2007). Tectonics, fracturing of rock, and erosion. *Journal of Geophysical Research*, *112*(F3), F03014. https://doi.org/10.1029/2005jf000433

Mooney, W. D., Barrera-Lopez, C., Suárez, M. G., & Castelblanco, M. A. (2023). Earth crustal model 1 (ECM1): A 1 x 1 global seismic and density model. *Earth-Science Reviews*, *243*, 104493. https://doi.org/10.1016/j.earscirev.2023.104493

Nábělek, J., Hetényi, G., Vergne, J., Sapkota, S., Kafle, B., Jiang, M., et al. (2009). Underplating in the Himalaya-Tibet collision zone revealed by the Hi-CLIMB experiment. *Science*, *325*(5946), 1371–1374. https://doi.org/10.1126/science.1167719

Naliboff, J. B., Conrad, C. P., & Lithgow-Bertelloni, C. (2009). Modification of the lithospheric stress field by lateral variations in plate-mantle coupling. *Geophysical Research Letters*, *36*(22), L22307. https://doi.org/10.1029/2009gl040484

Naliboff, J. B., Lithgow-Bertelloni, C., Ruff, L. J., & de Koker, N. (2012). The effects of lithospheric thickness and density structure on Earth's stress field. *Geophysical Journal International*, *188*(1), 1–17. https://doi.org/10.1111/j.1365-246x.2011.05248.x

Neres, M., Neves, M. C., Custódio, S., Palano, M., Fernandes, R., Matias, L., et al. (2018). Gravitational potential energy in Iberia: A driver of active deformation in high-topography regions. *Journal of Geophysical Research: Solid Earth*, *123*(11), 10–277. https://doi.org/10.1029/2017jb015002

Nicol, A., Walsh, J., Childs, C., & Manzocchi, T. (2020). The growth of faults. In *Understanding faults* (pp. 221–255). Elsevier.

Reiter, K. (2021). Stress rotation–impact and interaction of rock stiffness and faults. *Solid Earth*, *12*(6), 1287–1307. https://doi.org/10.5194/se-12-1287-2021

Schumm, S. A., Dumont, J. F., & Holbrook, J. M. (2000). *Active Tectonics and Alluvial Rivers* (Vol. 276). Cambridge University Press.

Simpson, R. W. (1997). Quantifying Anderson's fault types. *Journal of Geophysical Research*, *102*(B8), 17909–17919. https://doi.org/10.1029/97jb01274

Stamps, D. S., Flesch, L. M., Calais, E., & Ghosh, A. (2014). Current kinematics and dynamics of Africa and the East African Rift system. *Journal of Geophysical Research: Solid Earth*, *119*(6), 5161–5186. https://doi.org/10.1002/2013jb010717

Stixrude, L., & Lithgow-Bertelloni, C. (2005). Thermodynamics of mantle minerals—I. Physical properties. *Geophysical Journal International*, *162*(2), 610–632. https://doi.org/10.1111/j.1365-246x.2005.02642.x

Styron, R., & Pagani, M. (2020). The GEM global active faults database. *Earthquake Spectra*, *36*(1suppl), 160–180. https://doi.org/10.1177/8755293020944182

Sylvester, A. G. (1988). Strike-slip faults. *Geological Society of America Bulletin*, *100*(11), 1666–1703. https://doi.org/10.1130/0016-7606(1988)100<1666:ssf>2.3.co;2

Vita-Finzi, C. (2012). River history and tectonics. *Philosophical Transactions of the Royal Society A: Mathematical, Physical and Engineering Sciences*, *370*(1966), 2173–2192. https://doi.org/10.1098/rsta.2011.0605

Wang, C.-Y., Flesch, L. M., Silver, P. G., Chang, L.-J., & Chan, W. W. (2008). Evidence for mechanically coupled lithosphere in central Asia and resulting implications. *Geology*, *36*(5), 363–366. https://doi.org/10.1130/g24450a.1

Wibberley, C. A., & Shimamoto, T. (2005). Earthquake slip weakening and asperities explained by thermal pressurization. *Nature*, *436*(7051), 689–692. https://doi.org/10.1038/nature03901

Willett, S. D., McCoy, S. W., Perron, J. T., Goren, L., & Chen, C.-Y. (2014). Dynamic reorganization of river basins. *Science*, *343*(6175), 1248765. https://doi.org/10.1126/science.1248765

Wobus, C., Whipple, K. X., Kirby, E., Snyder, N., Johnson, J., Spyropolou, K., et al. (2006). Tectonics from topography: Procedures, promise, and pitfalls.

Wu, H., Kimball, J. S., Li, H., Huang, M., Leung, L. R., & Adler, R. F. (2012). A new global river network database for macroscale hydrologic modeling. *Water Resources Research*, *48*(9), W09701. https://doi.org/10.1029/2012wr012313

Yin, A., & Taylor, M. H. (2011). Mechanics of V-shaped conjugate strike-slip faults and the corresponding continuum mode of Continental deformation. *Bulletin*, *123*(9–10), 1798–1821. https://doi.org/10.1130/b30159.1

Yuan, D., Ge, W., Chen, Z., Li, C., Wang, Z., Zhang, H., et al. (2013). The growth of northeastern Tibet and its relevance to large-scale continental geodynamics: A review of recent studies. *Tectonics*, *32*(5), 1358–1370. https://doi.org/10.1002/tect.20081

Zhong, S., Zuber, M. T., Moresi, L., & Gurnis, M. (2000). Role of temperature-dependent viscosity and surface plates in spherical shell models of mantle convection. *Journal of Geophysical Research*, *105*(B5), 11063–11082. https://doi.org/10.1029/2000jb900003

Zoback, M. L. (1992). First-and second-order patterns of stress in the lithosphere: The world stress map project. *Journal of Geophysical Research*, *97*(B8), 11703–11728. https://doi.org/10.1029/92jb00132

Zoback, M. L., & Burke, K. (1993). Lithospheric stress patterns: A global view. *Eos, Transactions American Geophysical Union*, *74*(52), 609–618. https://doi.org/10.1029/93eo00340